A&A, 708, A250 (2026)
https://doi.org/10.1051/0004-6361/202658894

Astronomy & Astrophysics

Calibration of the [C/N] and [Y/Mg] chemical clocks with asteroseismic ages from the TESS space mission

E. Pakštienė[1,⋆], G. Tautvaišienė[1], V. Bagdonas[1], H. Kjeldsen[2], M. L. Winther[2], A. Drazdauskas[1], C. Viscasillas Vázquez[1], Y. Chorniy[1], Š. Mikolaitis[1], R. Minkevičiūtė[1], and E. Stonkutė[1]

[1] Institute of Theoretical Physics and Astronomy, Vilnius University, Saulėtekio av. 3, 10257 Vilnius, Lithuania
[2] Stellar Astrophysics Centre, Department of Physics and Astronomy, Aarhus University, Ny Munkegade 120, 8000 Aarhus, Denmark

Received 8 January 2026 / Accepted 12 February 2026

ABSTRACT

Context. Stellar ages are typically very difficult to estimate for field stars. New empirical methods, based on abundance ratios of chemical elements, are emerging and need to be calibrated.
Aims. Our main aim is to contribute to revealing relations between [C/N] and [Y/Mg] ratios and stellar ages by determining asteroseismic ages and non-local thermodynamic equilibrium (NLTE) abundances, and accounting for stellar evolutionary stages and birth places in the Galaxy.
Methods. We searched for solar pulsations in a sample of 1250 bright F, G, and K giants using data from the TESS space telescope and determined asteroseismic ages using the BASTA and PARAM codes. For the [Y/Mg] relations with age, we determined abundances accounting for deviations from the local thermodynamic equilibrium. For the [C/N] relations with age, we separated stars according to their evolutionary stages.
Results. We determined asteroseismic ages for 218 giants and derived [Y/Mg] and [C/N] relations with age for subsamples of stars in three regions of the Galactic thin disc and the thick disc.
Conclusions. The [Y/Mg]–age relation exhibits a clear radial dependence across the Galactic disc, with a steeper trend in the outer disc, progressively flatter relations towards the inner disc, and a very flat trend in the thick disc. NLTE abundances of Mg and especially of Y have to be used in order to obtain a more precise stellar age evaluation from [Y/Mg] ratios. When using [C/N] abundance ratios as stellar age indicators, evolutionary stages of stars have to be taken into account.

Key words. stars: abundances – stars: evolution – galaxy: disk

1. Introduction

Age, a parameter describing how much time has passed since the birth of any object or since a specific event took place, is one of the most important parameters in astronomy. In order to paint the picture of the evolution of the Universe, it is crucial to constrain ages and timescales of basically anything that has ever existed. Only then can we properly investigate the nature of which we are part.

Unfortunately, precise ages of objects and events in the Universe are debatable in relation to their fundamentals. The best example is probably the age of the Universe, or, in other words, how much time has passed since the Big Bang. With the help of advancing technology, the Planck Collaboration VI (2020) has managed to set the age of the Universe at 13.797 billion years. However, there are studies proposing a much older age (e.g. Gupta 2023; Llorente de Andrés 2024). The Milky Way has its own time-related mysteries as well. For example, it is still unclear when its main structural elements –thin and thick discs-formed (Kilic et al. 2017; Xiang & Rix 2022).

The best way to determine the ages of larger structures is to investigate its constituents, in this case the stars. However, many shortcomings do exist here as well. In stellar physics, the most common age determination methods have always been isochrone based, yet, even with most modern tools, these methods provide results with quite large uncertainties, sometimes spanning several billion years, making precise galactic investigations impossible (Soderblom 2010).

Another alternative for determining stellar age is based on asteroseismology (e.g. Aerts 2021). In this method, stellar oscillations of various stars are used to infer stellar ages. However, it has its own shortcomings – stellar oscillations cannot be detected in all stars. Nevertheless, this method is much more precise than others, and since the start of the NASA Transiting Exoplanet Survey Satellite (TESS, Ricker et al. 2015) space mission, covering almost all the sky, tens of millions of light curves have been collected; thus, ages determined from asteroseismology will continue to grow.

During the last decade, a new empirical method for the age determination has been extensively studied. This so-called chemical-clock method relies on astrospectroscopy, in particular, on stellar chemical abundances and their ratios, some of which have been noticed can, more or less, indicate stellar ages (e.g. da Silva et al. 2012; Salaris et al. 2015; Nissen 2015, 2016; Spina et al. 2016; Tucci Maia et al. 2016; Adibekyan et al. 2016; Lagarde et al. 2017; Slumstrup et al. 2017; Spina et al. 2018; Casali et al. 2019; Delgado Mena et al. 2019; Titarenko et al. 2019; Casali et al. 2020; Jofré et al. 2020; Tautvaišienė et al. 2021; Spoo et al. 2022; Viscasillas Vázquez et al. 2022; Shejeelammal et al. 2024; Vitali et al. 2024; Molero et al. 2025; Roberts et al. 2025; Tautvaišienė et al. 2025). However, this empirical method is not trivial as abundances of various

⋆ Corresponding author: erika.pakstiene@tfai.vu.lt

chemical elements found in stars are a function of many known and still unknown parameters. Abundance ratios are noted to be different in objects of different ages, metallicities, and galactic structural components (Masseron & Gilmore 2015; Casali et al. 2020; Tautvaišienė et al. 2021; Viscasillas Vázquez et al. 2022; Roberts et al. 2025).

Presently, the best identified chemical-element ratios used in chemical-clock methods are of *s*- and α-process origins, especially [Y/Mg] (Nissen 2015; Casali et al. 2020; Tautvaišienė et al. 2021; Viscasillas Vázquez et al. 2022). The reason for this is that the *s* process, while responsible for a wide range of elements and being of rather different origins, mostly occurs on longer timescales, and its effect is most apparent in younger objects. In contrast, enrichment of the interstellar medium with α elements progressed on much shorter timescales. Therefore, the ratio of $[s/\alpha]$ shows a prominent relationship with age. However, the calibration of this ratio as a chemical clock requires further efforts and large samples of different objects.

Recent studies also demonstrated that ratios of mixing-sensitive chemical elements, carbon and nitrogen, can also be used in age inference; however, this is only for stars after the first dredge-up (1DUP) (Salaris et al. 2015; Martig et al. 2016; Lagarde et al. 2017; Casali et al. 2019; Spoo et al. 2022; Tautvaišienė et al. 2025). It was also noticed that evolution stages of stars after the 1DUP have to be taken into account as well (Tautvaišienė et al. 2025, and references therein) since C and N abundances change during the path of stars through its evolutionary track. The first changes occur during the 1DUP (Iben 1965), when in the low-mass stars the isotopes of ^{13}C and ^{14}N are brought to the surface, while ^{12}C diffuses inwards, resulting in the reduction of ^{12}C/^{13}C and C/N ratios. In stars with masses below $\sim$2.2 $M_{\odot}$, these ratios decline further after the red giant branch (RGB) luminosity bump because of the extra-mixing processes start acting and last at least until the tip of the RGB (e.g. Lagarde et al. 2019). Thus, the different behaviour of C and N abundances may serve as stellar age indicators in red giants.

The current situation is that both [Y/Mg] and [C/N] show potential to be useful age indicators; however, their age relations are not confined enough with respect to galactic locations, metallicities, and other parameters. The ability to determine ages from asteroseismology will allow us to define various chemical-clock relations with higher precision. Thus, asteroseismic ages and high-resolution spectral abundance investigations are needed.

In this paper, we present ages determined using asteroseismic data from the TESS space telescope. In our study, we investigated [Y/Mg] and [C/N] ratios as chemical clocks, taking into account stellar evolutionary phases, mean galactocentric distances, and thin- and thick-disc attributions.

2. Stellar sample and method of analysis

In this study, we targeted 1250 F, G, and K spectral type stars with $V < 8$ mag in a field of about 45 deg radius centred on the TESS continuous viewing zone (CVZ) in the Northern Hemisphere. The stellar atmospheric parameters and abundances of chemical elements for this study were taken from Tautvaišienė et al. (2020), Tautvaišienė et al. (2021), and Tautvaišienė et al. (2022), hereafter called Paper I, Paper II, and Paper III. Only yttrium abundances for 110 stars had to be determined additionally in this work using the archival stellar spectra of the same Paper I and Paper III, and the ages were determined using data from the TESS space mission.

The observations in Paper I and Paper III were carried out with the Vilnius University Echelle Spectrograph (VUES) (Jurgenson et al. 2014, 2016) mounted on the Moletai Astronomical Observatory $f/12$ 1.65 m Ritchey–Chretien telescope. The VUES is a multi-mode spectrograph that covers a wavelength range from 4000 to 8800 Å. A spectral resolution mode with $R \sim 68\,000$ was used for observations of M spectral-type stars, and a mode with $R \sim 36\,000$ was used for other objects. The list contains no double-line spectroscopic binaries or stars rotating faster than 25 km s^{-1}.

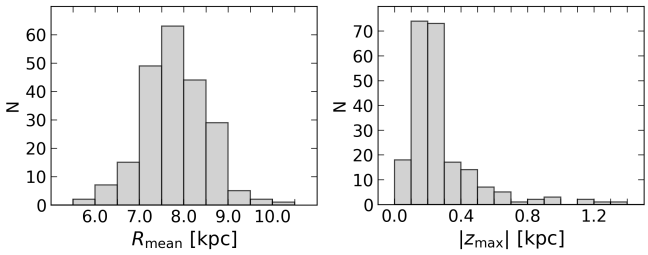

Fig. 1. Distribution of stars according to mean galactocentric distance, R_{mean}, and maximum height from the Galactic plane, $|z_{max}|$.

2.1. Galactocentric distances and isochronal ages

In this study, we also used the mean galactocentric distances (R_{mean}), the maximum distance from the Galactic plane ($|z_{max}|$), and the isochronal ages taken from Paper I and Paper III. In these studies, the kinematic parameters were computed using the Python-based package *galpy* (Bovy 2015) by integrating orbits for 5 Gyr within the default MWPotential2014. The Solar parameters of $R_{\odot} = 8$ kpc and $V_{circ} = 220$ km s^{-1} (Bovy et al. 2012), with a distance from the Galactic plane of $z_{\odot} = 0.02$ kpc (Joshi 2007) and the solar motion relative to the LSR adopted from Schönrich et al. (2010). While Paper I used the input data from *Gaia* DR2 (Luri et al. 2018; Katz et al. 2019; Gaia Collaboration 2016, 2018), Paper III used the photogeometric distances from Bailer-Jones et al. (2021) alongside the radial velocities of *Gaia* DR3 (Gaia Collaboration 2016, 2018; Lindegren et al. 2021; Seabroke et al. 2021). In both cases, uncertainties were estimated via 1000 Monte Carlo calculations, taking into account uncertainties in the input parameters. Figure 1 shows the distributions of the investigated stars according to their R_{mean} and $|z_{max}|$.

The isochronal ages were used in this work for comparison only. They were also taken from Paper I and Paper III, in which they were determined with a UniDAM code by Mints & Hekker (2017). This code combines spectroscopic data with infrared photometry from 2MASS (Skrutskie et al. 2006) and AllWISE (Cutri et al. 2021) and compares them with PARSEC (Bressan et al. 2012) isochrones to derive probability density functions (PDFs) for ages. The maximum error allowed for age was 3 Gyr. The mean uncertainty of the age determination calculated from the uncertainties of individual stars was $\sim$2 Gyr, the mean uncertainty of the R_{mean} determinations was $\sim$0.2 kpc, and the mean uncertainty of the $|z_{max}|$ determinations was $\sim$0.05 kpc.

2.2. Stellar atmospheric parameters and abundances of chemical elements

The stellar atmospheric parameters (effective temperature T_{eff}, surface gravity $\log g$, metallicity [Fe/H], and microturbulent velocity v_t) in Paper I and Paper III were determined from the equivalent widths of Fe I and Fe II lines using standard spectroscopic techniques. The effective temperatures were derived by

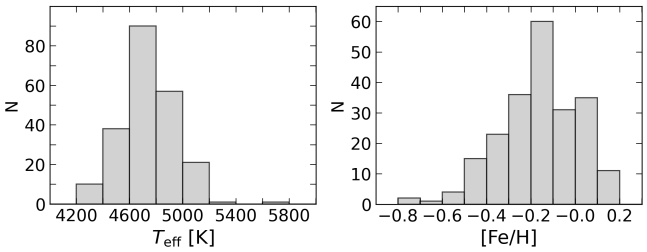

Fig. 2. Distribution of stars according to $T_{\rm eff}$ and [Fe/H].

minimising the slope of the abundances determined from Fe I lines with different excitation potentials. Surface gravities were found by requiring Fe I and Fe II lines to give the same iron abundances. The microturbulent velocity values were attributed by requiring Fe I lines to give the same iron abundances regardless of their equivalent widths. In total, 299 Fe I and Fe II lines were used to calculate the stellar atmospheric parameters with the tenth version of the MOOG code (Sneden 1973) and the MARCS[1] grid of constant flux local thermodynamic equilibrium (LTE) stellar atmosphere models (Gustafsson et al. 2008). The calculated medians of atmospheric parameter determination errors from all the stars in our sample are the following: $\sigma T_{\rm eff}$ = ±46 K; and $\sigma \log g$ = ±0.30, σ[Fe/H] = ±0.11, and $\sigma v_{\rm t}$ = ±0.27 km s^{-1}. Figure 2 shows the distribution of stars according to $T_{\rm eff}$ and [Fe/H].

Abundances of carbon, nitrogen, magnesium, and yttrium were also taken from Paper I, Paper II, and Paper III; however, additional abundance determinations for yttrium were made for 110 stars using the same method of analysis. Abundances of the investigated chemical elements were determined using spectral synthesis. For modelling of synthetic spectra, we used a spectrum synthesis code Turbospectrum (Alvarez & Plez 1998; Plez 2012). The analysis was carried out differentially with respect to the Sun, whereby a line-by-line investigation was applied. As the target stars were observed using two resolutions (~36 000 and ~68 000), their spectra were investigated differentially to the solar spectra observed in the corresponding resolution mode. The abundances were averaged from several observations, if available. Individual uncertainties in determining the atmospheric parameters and abundances of chemical elements are presented in Paper I, Paper II, and Paper III.

2.2.1. Non-local thermodynamic equilibrium effects

For the robustness of the study, we paid special attention to accounting for non-local thermodynamic equilibrium (NLTE) effects. As we focused on [C/N] and [Y/Mg], it is worth mentioning that C_2 bands that were used to determine the carbon abundance are not sensitive to NLTE deviations (Clegg et al. 1981; Gustafsson et al. 1999). The 6300.3 Å oxygen forbidden line used in the analysis is known to be unaffected by NLTE and shows little sensitivity to 3D effects (Asplund 2004; Pereira et al. 2009). This line forms nearly in LTE and is only weakly sensitive to convection; its formation is similar in 3D radiation hydrodynamic and 3D magnetohydrodynamic solar models (Bergemann et al. 2021). Therefore, possible NLTE effects on [C/N] should be very small. However, for magnesium and yttrium abundances we decided to compute the NLTE corrections according to Storm & Bergemann (2023) and Storm et al. (2024) for Y II and according to Bergemann et al. (2017) for Mg I using the updated Turbospectrum code (Gerber et al. 2023). As in Adibekyan et al. (2017), the NLTE effects on the [Mg/H] ratios in the investigated metallicity interval are small; however, for [Y/H] they reach ~0.1 dex. The dependencies are illustrated in Fig. 3.

[1] http://marcs.astro.uu.se/

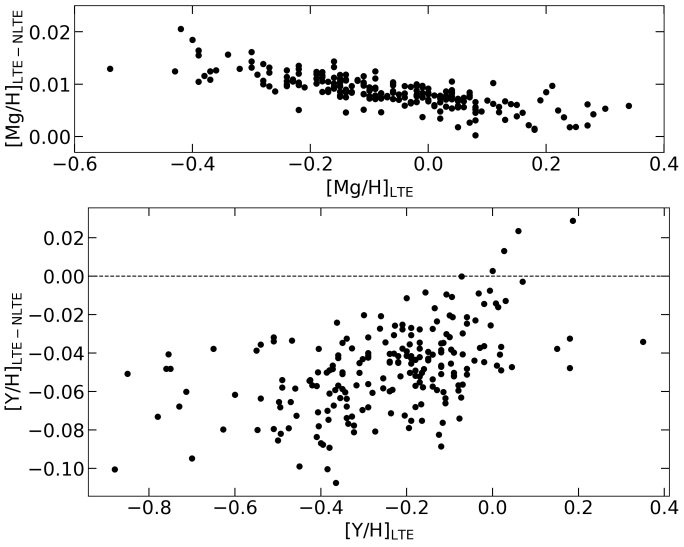

Fig. 3. NLTE corrections of [Mg/H] and [Y/H] for the investigated stars.

2.3. Asteroseismic ages

We analysed 30-minute and two-minute cadence TESS light curves of our set of stars observed in sectors 13–26. For targets observed with the 30-minute cadence, which constituted the majority of the analysed sample, the light curves were extracted from the TESS full-frame images using the TESS-Cut service (Brasseur et al. 2019) using the Lightkurve package (Lightkurve Collaboration 2018). For targets observed with two-minute cadence, the calibrated light curves were retrieved via the TESS bulk-download service, based on products generated by the SPOC pipeline (Jenkins et al. 2016). The light curves were de-trended and sigma clipped using a combination of standard procedures available within the Lightkurve package and custom routines developed by the authors when the default de-trending methods were found to be insufficient for asteroseismic analysis. Light curves from all available sectors were combined prior to analysis to improve the signal-to-noise ratio and frequency resolution, which is particularly important for low-frequency oscillations in red giant stars. Power spectra were computed from the de-trended combined light curves using the standard Fourier-based methods implemented in the Lightkurve package. The resulting power spectral densities were visually inspected to assess data quality and to confirm the presence of oscillation power excess. The frequency at maximum oscillation power ($\nu_{\rm max}$) was estimated by fitting a Gaussian profile to the continuum-flattened power spectrum and identifying the frequency corresponding to the peak of the fit. The large frequency separation ($\Delta\nu$) was determined using the autocorrelation of the power spectrum in the frequency region around $\nu_{\rm max}$ and subsequently manually verified using échelle diagrams. The uncertainty in $\nu_{\rm max}$ was estimated from the full width at half maximum (FWHM) of the fitted Gaussian envelope of the oscillation power excess. The uncertainty in $\Delta\nu$ was estimated from the width of the autocorrelation peak and by visual inspection of the corresponding échelle diagram.

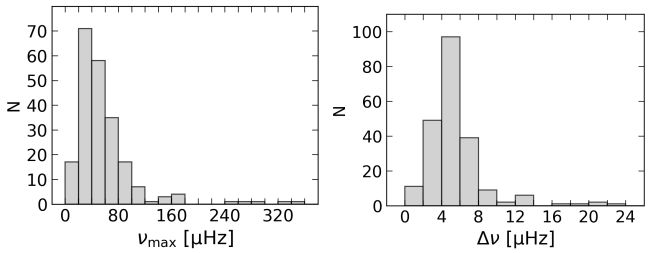

Fig. 4. Distribution of stars according to frequency at maximum power, ν_{max}, and the large frequency separation, $\Delta\nu$, derived in this study.

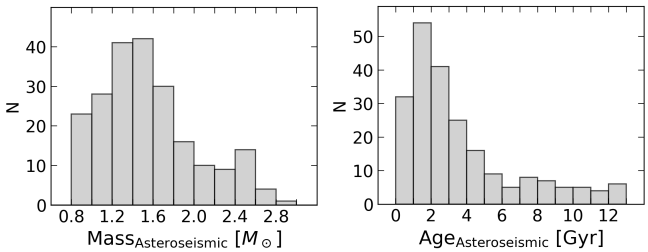

Fig. 5. Distribution of stars according to their asteroseismic masses and ages determined in this study.

This enabled us to obtain the pulsation spectra of all our stars; however, robust determinations of ν_{max} and $\Delta\nu$ were possible for only 218 stars. Only stars exhibiting clear solar-like pulsations with easily recognisable ridges of ℓ = 0, 1, and 2 modes in echelle diagrams were selected for further analysis and age determination. The derived asteroseismic parameters were visually checked for each star to evaluate their reliability and corrected if necessary. We were unable to determine the values of ν_{max} and $\Delta\nu$ for stars with $T_{eff} < 4200$ K and $T_{eff} > 5200$ K, and with $\log g < 2$ and $\log g > 3.4$. For other stars, the success rate of robust determination of asteroseismic parameters depended on the number of pointings. In the CVZ, it was about 60%; while in the area around it, it was about 20%. Consequently, the number of stars with asteroseismic ages determined was lower than we expected; however, it was sufficient to achieve the aims of this study. Figure 4 shows the distribution of stars with ν_{max} and $\Delta\nu$ determined.

Using ν_{max}, $\Delta\nu$, and the spectroscopic effective temperature T_{eff}, we calculated the initial approximate stellar mass, radius, $\log g$, and luminosity based on classical scaling relations (Kjeldsen & Bedding 1995):

$$\frac{M}{M_\odot} \simeq \left(\frac{\nu_{max}}{\nu_{max,\odot}}\right)^3 \left(\frac{\Delta\nu}{\Delta\nu_\odot}\right)^{-4} \left(\frac{T_{eff}}{T_{eff,\odot}}\right)^{3/2}, \quad (1)$$

$$\frac{R}{R_\odot} \simeq \left(\frac{\nu_{max}}{\nu_{max,\odot}}\right) \left(\frac{\Delta\nu}{\Delta\nu_\odot}\right)^{-2} \left(\frac{T_{eff}}{T_{eff,\odot}}\right)^{1/2}, \quad (2)$$

$$\log g \simeq \log\left(g_\odot \left(\frac{M}{M_\odot}\right)\left(\frac{R_\odot}{R}\right)^2\right), \quad (3)$$

$$\frac{L}{L_\odot} \simeq \left(\frac{R}{R_\odot}\right)^2 \left(\frac{T_{eff}}{T_{eff,\odot}}\right)^4. \quad (4)$$

Then, two computing codes were used to determine the asteroseismic age and precise stellar parameters. The first was an online interface PARAM (v.1.5) for the Bayesian estimation of stellar parameters (da Silva et al. 2006; Rodrigues et al. 2014, 2017), and the second was the BAyesian STellar algorithm (BASTA; Silva Aguirre et al. 2015; Aguirre Børsen-Koch et al. 2022).

2.3.1. Age determinations with PARAM

The parameters used for the age calculations in PARAM included ν_{max}, $\Delta\nu$, spectroscopic T_{eff}, and metallicity [Fe/H], along with asteroseismic $\log g$ and luminosity $L/L_\odot$ (both calculated using scaling relations (3) and (4), which helped to reduce age-determination uncertainties and did not materially change output values). We assumed the solar seismic parameters $\nu_{max,\odot}$ = 3141 μHz and $\Delta\nu_\odot$ = 134.98 μHz (Fredslund Andersen et al. 2019), a solar metal content of $Z_\odot$ = 0.01756 (Paxton et al. 2011, 2013), an exponential initial mass function (Chabrier 2001), and an unknown prior of the evolutionary stage. To account for the mass loss in our calculations, we applied a Reimers-type mass-loss efficiency coefficient, η_R = 0.4. This value reflects the average value of the Reimers coefficient well considering different empirical contexts and models (McDonald & Zijlstra 2015; Valle et al. 2018).

The ages were determined using a grid of MESA isochrones (Rodrigues et al. 2017), where individual radial mode frequencies and large separations, $\Delta\nu$, were calculated for each model of the grid. As the PARAM description states that MESA isochrones are available in the mass range of $0.6 \leq M/M_\odot < 2.5$, for stars with a scaling relation mass greater than 2.5 $M_\odot$ (up to 4 $M_\odot$), the age was calculated with the PARSEC isochrones instead. Finally, a two-step Bayesian method (Rodrigues et al. 2014) was used to determine the ages of our selected stars. Using this method, the ages were determined for 218 stars.

2.3.2. Age determinations with BASTA

This algorithm uses grid-based modelling to compare the observed parameters of the stars with stellar models and to infer the parameters of the stars using Bayesian statistics. Here, the observables used were the spectroscopic effective temperature, T_{eff}; metallicity, [Fe/H]; frequency of maximum power, ν_{max}; and large frequency separation, $\Delta\nu$, determined in this study.

The observations were compared to the BaSTI isochrones (Hidalgo et al. 2018; Pietrinferni et al. 2021), specifically case 4 in Table 1 of Aguirre Børsen-Koch et al. (2022), where the effects of overshooting, diffusion, and mass-loss are included in the models. Here, the model-predicted value of ν_{max} was determined using the classical scaling relations (Eq. (10), Kjeldsen & Bedding 1995), and the model-predicted value of $\Delta\nu$ was calculated using the corrected scaling relations of Sharma et al. (2016) and Stello & Sharma (2022). Using this method, the ages were determined for 182 stars, given as the median, 16th, and 84th quantiles of the posterior age distribution, as listed in Table A.1 (Cols. 4–6).

Figure 5 shows the mass and age distributions of the 218 stars investigated based on asteroseismic data from the TESS telescope. The masses and ages determined using PARAM and BASTA software were averaged.

2.4. Evolutionary stages

For the use of C and N for the stellar age evaluation, we had to define evolutionary stages of stars (see Tautvaišienė et al. 2025). With this purpose in mind, asteroseismology helps significantly.

At later stages of stellar evolution, such as the red giant branch (RGB) and helium-core-burning phases – the red clump

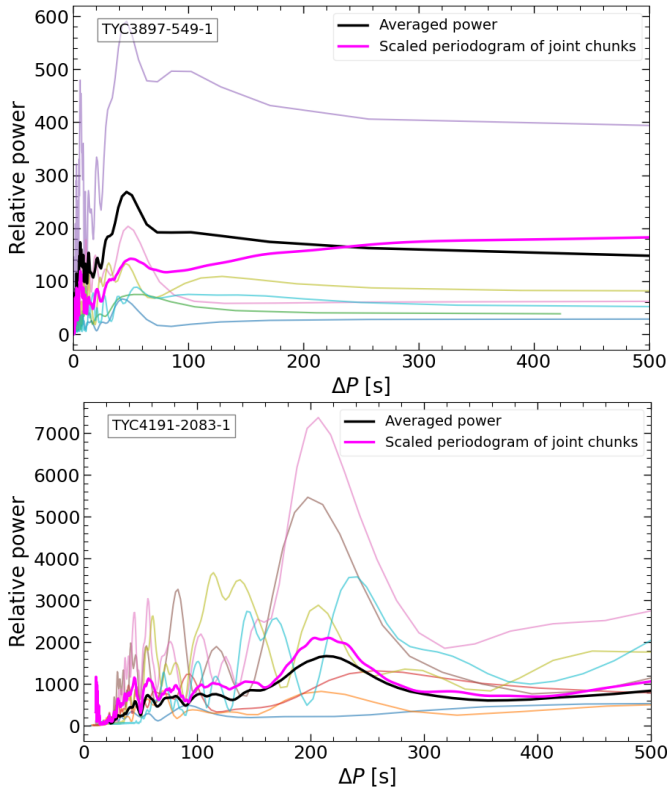

Fig. 6. Examples of 'periodograms of periodograms' for the RGB star TYC3897-549-1 and the RC star TYC4191-2083-1.

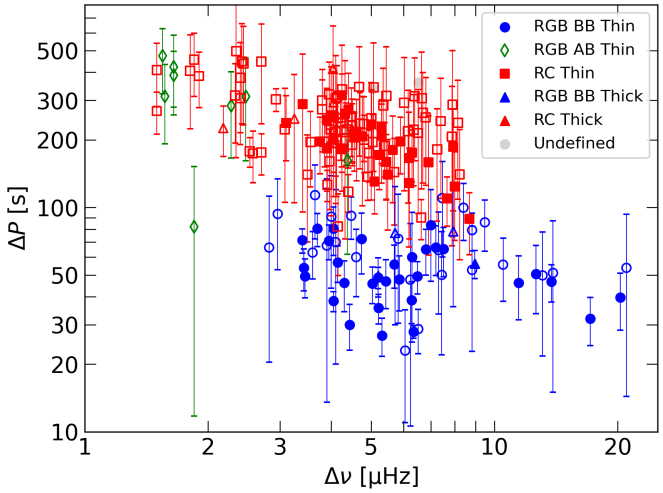

Fig. 7. Relation of ΔP and $\Delta\nu$ for the investigated stars. The blue symbols show giants below the RGB luminosity bump (BB), the green symbols are for giants above the bump (AB), and the red symbols are for red clump (RC) stars. The filled circles show stars for which the evolutionary stage was attributed with higher confidence. See the text for more explanations.

(RC) in the case of our sample – g modes originating in the deep stellar interior begin to influence surface p modes through mode coupling, creating detectable mixed modes (Beck et al. 2011). This coupling leads to characteristic period spacings (ΔP) between the consecutive mixed $\ell = 1$, reflecting the underlying g-mode structure. This period spacing, also called the bumped period spacing (e.g. Mosser et al. 2015), is particularly sensitive to the core structure, allowing the period spacing to reflect differences in burning processes, such as hydrogen-shell burning in RGB versus the core helium burning in RC stars. Studies revealed that the period spacings between consecutive $\ell = 1$ mixed modes are directly sensitive to the density gradient (or Brunt–Väisälä frequency profile) in the radiative zone between the core and convective envelope (Beck et al. 2011; Bedding et al. 2011; Mosser et al. 2012). The interpretation of period spacing as a function of stellar oscillations has been confirmed and refined in subsequent studies (e.g. Mosser et al. 2014; Mosser et al. 2018).

In stars undergoing hydrogen shell burning on the RGB, the buoyancy frequency structure leads to relatively small period spacing ($\Delta P \approx$ 30–80 s). In contrast, ΔP in stars undergoing helium burning in the core on the horizontal branch or in the red clump is larger ($\Delta P \gtrsim 100$ s) due to differences in the core structure and surrounding stratification. This distinction provides a robust way to identify the evolutionary stage of red giants (Bedding et al. 2011).

Thus, we analysed the $\ell = 1$ pulsation mode regions in the pulsation periodograms to determine the most likely ΔP value. For this purpose, we computed a periodogram for each selected spectral chunk containing split $\ell = 1$ modes (pale coloured curves in Fig. 6), as well as their averaged periodogram of periodograms, and that obtained from the combined chunks (see Fig. 6). Period spacing values were obtained for 177 stars, and the distribution of the resulting ΔP and $\Delta\nu$ is shown in Fig. 7. The results of higher confidence are marked with filled symbols. They represent 33 stars, for which the evolutionary stage was classified as giants below the RGB luminosity bump (RGB BB), and 32 stars were classified as RCs. For the remaining stars with ΔP of lower accuracy or without its determination, the evolutionary phases were inferred by involving investigations of stellar locations in the $\log g$ versus $T_{\rm eff}$ diagrams relatively to the corresponding evolutionary sequences. These stars are presented in the figures by the open symbols. From the evolutionary sequences, we also inferred nine stars in the evolutionary phase above the RGB luminosity bump (RGB AB). They are marked in the figures by the green diamonds. For 20 stars, the evolutionary stage remained undefined. They are marked in the figures by the grey symbols. The triangles show stars belonging to the thick disc.

It is interesting to note that among the 189 bright stars investigated in the TESS continuous viewing zone in our work, about 60% belong to the RC and 40% to the RGB. Very similar percentages of stars in these two evolutionary stages were identified among 395 fainter stars in the *Kepler* field by Bedding et al. (2011).

3. Results and discussion

In the machine-readable Table A.1, we provide the determined asteroseismic stellar ages, masses, $\nu_{\rm max}$ and $\Delta\nu$ values, NLTE [Mg/H] and [Y/H] abundances, the determined stellar evolutionary stages, and other parameters used in this study taken from Paper I, Paper II, and Paper III for convenience.

3.1. Comparison of asteroseismic and classical isochronal ages

The age determination of field giants is an extremely difficult task when using the traditional technique of matching the atmospheric parameters to stellar isochrones, as the isochrones with different parameters are located quite close to each other, or even overlap. To overcome this problem, additional observables to

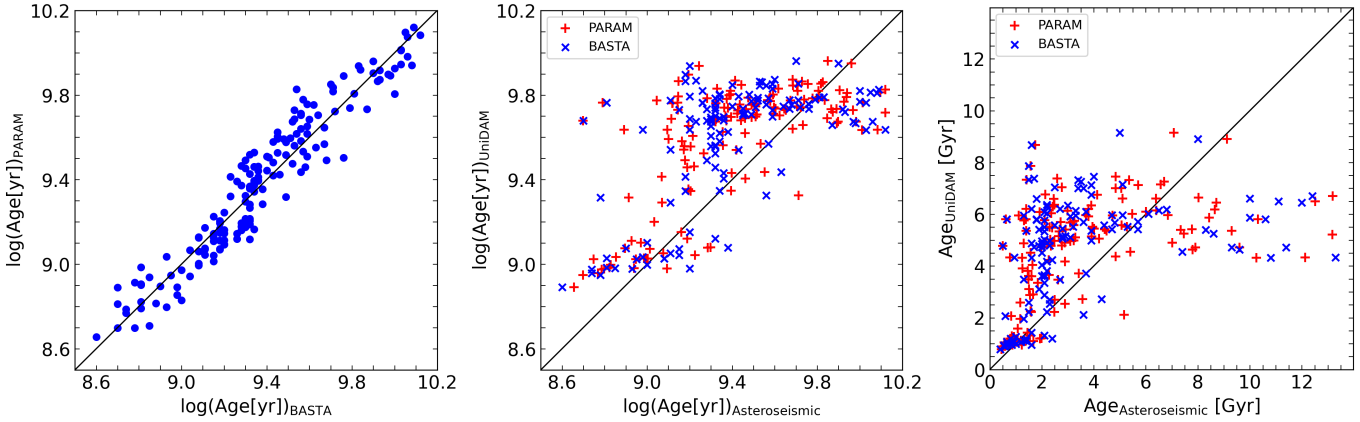

Fig. 8. Comparison of ages determined using PARAM (v.1.5), BASTA, and UniDAM softwares.

the effective temperature, surface gravity, and metallicity have been employed and tested with a statistical Bayesian approach (e.g. Jørgensen & Lindegren 2005; Mints & Hekker 2017). One such method, the UniDAM tool, uses spectroscopic data combined with infrared photometry and compares these in a Bayesian manner with PARSEC isochrones to derive probability density functions (PDFs) for stellar masses, ages, and distances. It treats PDFs of pre-helium-core-burning, helium-core-burning, and post-helium-core-burning solutions, as well as different peaks in multi-modal PDFs of the different stellar evolutionary phases separately (Mints & Hekker 2017). Using this tool, the ages were determined for all our sample of stars in Paper I and Paper III. We decided to compare the ages determined using the UniDAM tool with the ages determined in this work using two approaches, which involve very important asteroseismic observables.

In Fig. 8, we first compare the ages determined with the PARAM and BASTA tools (left panel) and see a rather good agreement. The middle panel shows the comparison of UniDAM ages with PARAM and BASTA ages on a logarithmic scale, and the right panel is presented on a linear scale for convenience. It is visible that with the UniDAM tool, the ages of young stars were overestimated, whereas for older stars, they were underestimated. Bearing in mind that solar-type oscillations are not detected in all giant stats, the classical methods have to be further developed, and maybe some new probability density functions could be adopted from asteroseismology to remove deviations. Other stellar age-determination methods, such as that of chemical clocks, investigated in this work, have also to be developed.

3.2. Relation of [Y/Mg] with age

To investigate possible radial dependencies in the $[Y/Mg]_{NLTE}$ and age relationship, we divided the sample into three subsamples according to the mean galactocentric radius of each star (R_{mean}). Stars with $R_{mean} < 7.5$ kpc were assigned to the inner disc, those with $7.5 \leq R_{mean} \leq 8.5$ kpc define the solar neighbourhood, and stars with $R_{mean} > 8.5$ kpc trace the outer disc, following commonly adopted radial divisions in the literature (e.g. Boeche et al. 2014; Hunt et al. 2015; Sysoliatina et al. 2018).

Thick-disc stars were treated as a separate population based on their chemical and kinematic properties. The separation into Galactic thin- and thick-disc components of our sample stars was done in Paper I and Paper III following the chemical and kinematic criteria defined in the Tinsley–Wallerstein and Toomre

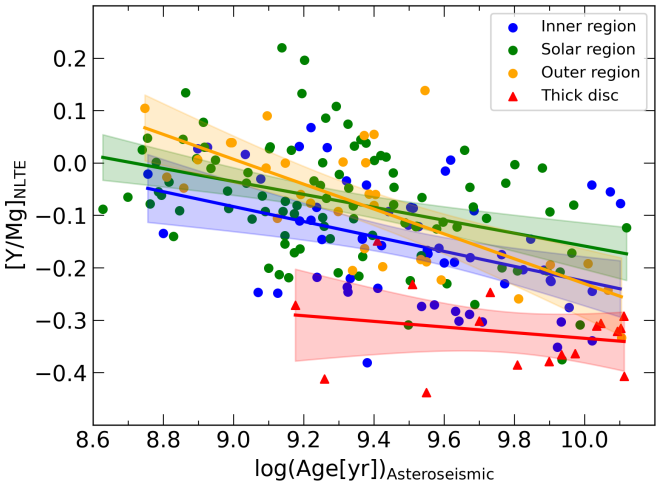

Fig. 9. [Y/Mg] as a function of stellar age for thin- and thick-disc stars. Linear fits for different Galactic regions and their 95% confidence intervals are shown. Stars with $R_{mean} < 7.5$ kpc are attributed to the inner Galactic disc, the solar region is at $7.5 \leq R_{mean} \leq 8.5$ kpc, and the outer disc is at $R_{mean} > 8.5$ kpc.

diagrams, as well as the age-chemo-kinematics approach proposed by Lagarde et al. (2021). This division allowed us to explore how the $[Y/Mg]_{NLTE}$–age relation varies across the Galaxy, and the resulting trends are shown together with their linear fits in Fig. 9.

A common feature of *s*-process chemical clocks is that their behaviour varies across the Galactic disc, reflecting differences in star-formation efficiencies and enrichment timescales. In our sample, this diversity is clearly visible in the $[Y/Mg]_{NLTE}$–age relations illustrated in Fig. 9 and quantified by the linear relations and Pearson correlation coefficients (PCC) for all four Galactic components (Eqs. (5)–(8)):

– Inner disc (61 stars)

$$\log \text{Age} = -7.042\,[Y/Mg]_{NLTE} + 8.444, \text{PCC} = -0.42, \quad (5)$$

– Solar region (98 stars)

$$\log \text{Age} = -8.13\,[Y/Mg]_{NLTE} + 8.74, \text{PCC} = -0.40, \quad (6)$$

– Outer disc (32 stars)

$$\log \text{Age} = -4.219\,[Y/Mg]_{NLTE} + 9.046, \text{PCC} = -0.70, \quad (7)$$

– Thick disc (17 stars)

$$\log \text{ Age} = -18.519\,[\text{Y/Mg}]_{\text{NLTE}} + 3.778, \text{PCC} = -0.23. \quad (8)$$

The outer disc shows the steepest decline with age (see Eq. (7)), pointing to a strong temporal evolution of the *s*-process contribution driven by slow star formation and extended enrichment histories. In addition to this steeper slope, the outer disc is systematically offset towards higher [Y/Mg] values at a fixed age, indicating a higher overall level of chemical enrichment. In contrast, the inner disc and the solar neighbourhood (Eqs. (5) and (6)) exhibit noticeably shallower trends and lower zero points, suggesting that rapid early evolution in these regions results in a reduced sensitivity of [Y/Mg] to stellar age. This behaviour is consistent with previous findings showing weaker [*s*-/α]–age relations and lower zero points at smaller galactocentric radii (Viscasillas Vázquez et al. 2022; Ratcliffe et al. 2024), based on open clusters from the Gaia-ESO Survey (Randich et al. 2022) and on large samples of disc field stars from APOGEE (Majewski et al. 2017) and GALAH (De Silva et al. 2015), respectively. However, the latest multi-zone chemical-evolution models, while able to reproduce the increase of [*s*-/α] with age in the outer regions, still fail to match the observed [Y/Mg] trends in the inner disc towards young ages (Molero et al. 2025). These models are based on the three-infall chemical-evolution framework with state-of-the-art nucleosynthesis prescriptions developed by Spitoni et al. (2023) and extended to the entire Galactic disc by Palla et al. (2024). From the stellar-evolution perspective, magnetic-buoyancy-induced mixing in asymptotic giant branch (AGB) stars may reduce yttrium production at high metallicity (Magrini et al. 2021), potentially explaining the low [Y/Mg] ratios in the inner disc.

The thick disc, however, displays an extremely weak dependence of $[\text{Y/Mg}]_{\text{NLTE}}$ on age and the lowest zero point (see Eq. (8)). The flat trend reflects its formation during a short and intense star-formation episode dominated by Type II supernovae, before low-mass AGB stars contributed significantly to the *s*-process enrichment, and the low zero point reflects its early formation. As a consequence, thick-disc stars retain uniformly low [Y/Mg] values and do not show a clear age signature, confirming that this ratio is not a reliable age indicator for this older population (Paper II). We also divided stars of the thin disc according to their maximum distance from the Galactic plane into three groups with $|z_{\text{max}}|$ from 0 to 0.2 kpc, from 0.2 to 0.4 kpc, and with distances larger than 0.4 kpc, but a negligible difference in the relations of [Y/Mg] with age was found.

With the aim of seeing how important it is to use the NLTE [Y/Mg] values and asteroseismic ages for the chemical clock's calibration, we compared $[\text{Y/Mg}]_{\text{NLTE}}$ and $[\text{Y/Mg}]_{\text{LTE}}$ relations with ages determined using asteroseismic data in this work and using the UniDAM software in Paper I and Paper III. In Fig. 10, we show the comparison for 99 stars in the solar region ($7.5 \leq R_{\text{mean}} \leq 8.5$ kpc). We can see systematic differences, which can lead to quite significant uncertainties in age determination. It is interesting that the relationship between $[\text{Y/Mg}]_{\text{LTE}}$ and UniDAM ages lies between NLTE and LTE [Y/Mg] and asteroseismic age relations.

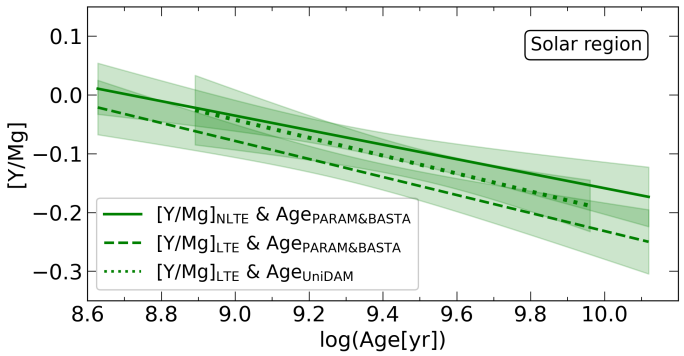

Fig. 10. Comparison of $[\text{Y/Mg}]_{\text{NLTE}}$ and $[\text{Y/Mg}]_{\text{LTE}}$ relations with ages determined using asteroseismic data (the continuous and dashed lines, respectively) and using the LTE [Y/Mg] values and ages computed with the UniDAM software (the dotted line). The relations are for the same 99 stars in the solar region at $7.5 \leq R_{\text{mean}} \leq 8.5$ kpc. The dashed relation was taken from Viscasillas Vázquez et al. (2025).

3.3. Relation of [C/N] with age

Figure 11 shows [C/N] dependence on stellar ages for stars at the lower part of the RGB and for helium-core-burning stars. Smaller subsamples, including stars of the upper part of RGB or the thick disc stars, are plotted but not used for calculations of the relations. The obtained [C/N] and age relations as presented in Fig. 11, the PCC coefficients, and the numbers of stars used for the calculations are the following:

– RGB stars below the RGB luminosity bump:

$$\log \text{Age} = 3.891\,[\text{C/N}] + 10.833, \text{PPC} = 0.63, \text{N} = 62, \quad (9)$$

– RC stars:

$$\log \text{Age} = 3.984\,[\text{C/N}] + 11.363, \text{PPC} = 0.66, \text{N} = 105. \quad (10)$$

In Fig. 11, we also plot the ralations taken from Tautvaišienė et al. (2025), which were determined using data from the *Gaia*-ESO survey for the first ascent giants below the RGB luminosity bump and for the helium-core-burning clump stars in 44 open clusters. Despite the lower accuracy of the [C/N] determinations in the field stars and possible misattribution to evolutionary stages, the agreement of the relations is very good. The relations determined using the open clusters cover younger ages, while our sample of field stars extend the relations to older ages well.

Recently, Roberts et al. (2025) used a much larger sample of stars with [C/N] determined in the Apache Point Observatory Galactic Evolution Experiment (APOGEE) Data Release 17 (Abdurro'uf et al. 2022) and used a polynomial function that includes [Fe/H] for the [C/N] relation with age. This approach needs to be further investigated. The fits received by Roberts et al. (2025) and our work agree well at log(Age[Gyr])~9.4. However, since the [C/N] values in that work even reached +0.1 dex for the oldest stars (log(Age[Gyr])~10), a polynomial fit was applied. A reason for applying the polynomial fit could be caused by the large number of merged stars in the APOGEE DR17 sample, which according to Lu et al. (2026) have [C/N] values from −0.05 – 0.2 dex. It would be interesting to check whether such large [C/N] values were also dominated by the thick-disc stars. In our work, the relations were only computed for thin-disc stars. Their [C/N] values at a similar age were not larger than ∼ −0.1 dex; therefore, the linear relation was sufficient. In a recent study by Spoo et al. (2025), both polynomial and linear relations were computed. They included [C/N] values of several metal-deficient globular clusters, and proposed that the same relation could be used in the [Fe/H] interval from −1.3 dex to +0.3 dex. However, as we see from the study by Roberts et al. (2025), the [C/N] values in more metal-deficient stars of the same age are higher. The metallicity interval in our study is

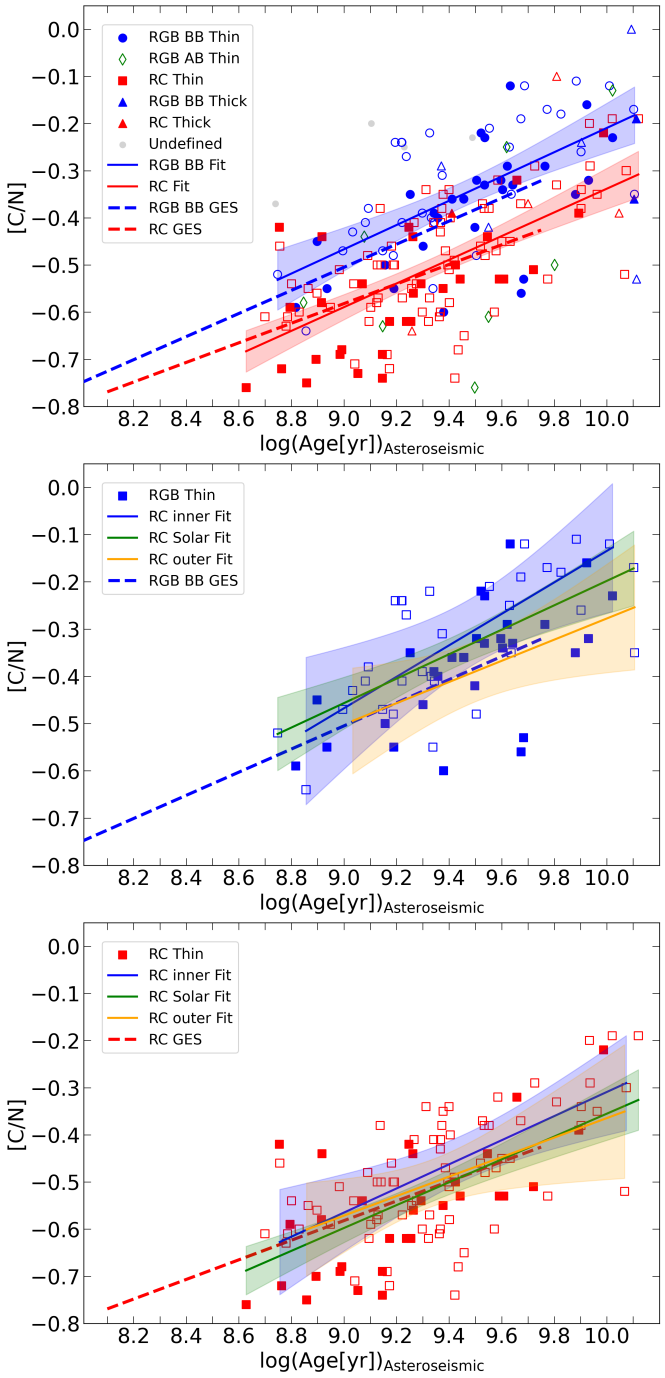

Fig. 11. Relation of [C/N] with asteroseismic age for stars at different evolutionary stages. The filled symbols are for stars with evolutionary stages determined with higher confidence. In the first plot, the solid blue relation is for the first ascent RGB stars, the red one is for RC stars, both are of the thin-disc stars. The shadowed areas show the confidence intervals of 95%. The corresponding relations from the *Gaia*-ESO Survey (Tautvaišienė et al. 2025) are shown for comparison by dashed lines. In the following two plots, the relations are shown for RGB and RC stars in the inner Galactic disc ($R_{\rm mean}$ < 7.5 kpc), in the Solar region (7.5 ≤ $R_{\rm mean}$ ≤ 8.5 kpc), and in the outer disc ($R_{\rm mean}$ > 8.5 kpc), respectively.

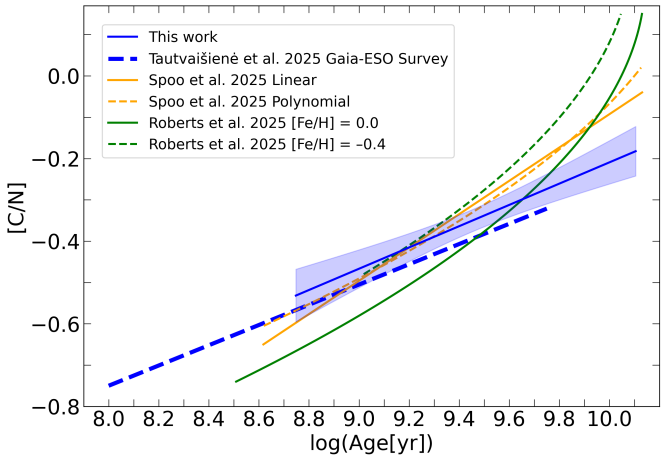

Fig. 12. Comparison of the recent [C/N] versus age relations for the 1DUP RGB stars. The blue line and the shadowed confidence interval of 95% show the relation computed in our work, the thick dashed line is from the *Gaia*-ESO survey open clusters (Tautvaišienė et al. 2025), the orange lines are from Spoo et al. (2025) for the polynomial and linear fits based on open and globular clusters, and the green lines are from Roberts et al. (2025) for the field stars of two different metallicities.

quite small, but we can infer this tendency as well. In Fig. 12, we show a comparison of [C/N] versus age relations for 1DUP RGB stars determined in our work and in recent studies by Roberts et al. (2025), Spoo et al. (2025), and Tautvaišienė et al. (2025). It is clear that further investigations including the information on the Galactic components, metallicity, and evolutionary stages of stars have to be performed.

In our work, we also checked the relationship of the [C/N] ratio with the mean galactocentric distance. As for the [Y/Mg] relation, we assigned stars with $R_{\rm mean}$ < 7.5 kpc to the inner disc, those with 7.5 ≤ $R_{\rm mean}$ ≤ 8.5 kpc to the solar neighbourhood, and stars with $R_{\rm mean}$ > 8.5 kpc to the outer disc. One may infer that in the inner regions of the Galactic disc, the [C/N] ratios in giant stars are less negative than in the Solar and outer regions because the initial abundances of CNO could be different. This possibility is supported, for example, by investigations of cepheids (Luck et al. 2011; Luck 2018) or H II regions (Arellano-Córdova et al. 2020). However, as seen from the two bottom panels in Fig. 11, the uncertainties in the [C/N] determinations and the limited samples of stars do not allow us to see significant differences. In a study of 1475 pre-dredge-up giants from APOGEE DR12 by Martig et al. (2016), no differences in [C/N] values were found in the inner and outer Galactic discs either. This question remains for further studies. We also divided stars of the thin disc according to their maximum distance from the Galactic plane into three groups with $|z_{\rm max}|$ from 0 to 0.2 kpc, from 0.2 to 0.4 kpc, and with distances larger than 0.4 kpc, but a negligible difference in the relations of [C/N] with age was found.

3.4. Comparison of C and N abundances with evolutionary models

Having a fairly large sample of giants in different evolutionary stages and accurate masses determined using asteroseismic data, it was interesting to compare the C/N abundance ratios with theoretical predictions. Fig. 13 shows the dependence of the C/N ratio on the stellar mass at different evolutionary stages and models that include alterations of C/N caused by the first dredge-up (Charbonnel et al. 2017), as well as by thermohaline-induced extra mixing (Lagarde et al. 2017) and by thermohaline- and rotation-induced extra mixing (Charbonnel et al. 2017). In Fig. 13, we can see that the C/N abundance ratios in the majority of investigated first-ascent RGB stars are affected by the

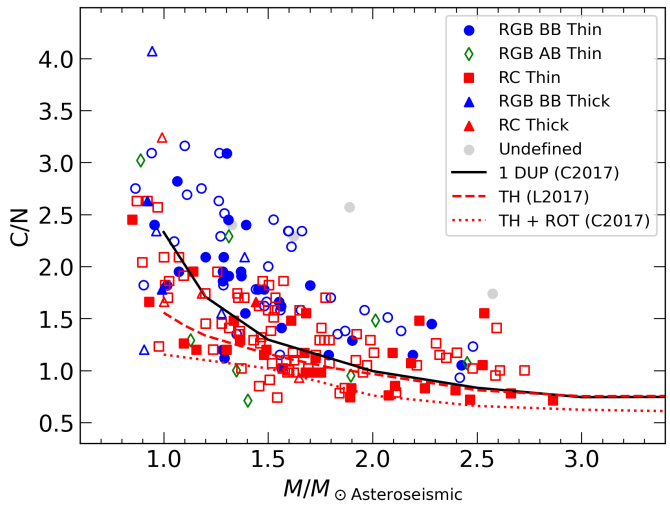

Fig. 13. Comparison of C/N ratios of investigated stars with theoretical models for solar-metallicity stars. The filled symbols are for stars with evolutionary stages determined with higher confidence. The solid black line represents the C/N ratios predicted by the model for stars after the 1 DUP, taken from Charbonnel et al. (2017). The dashed red line represents the minimal values in the model with thermohaline-induced extra mixing (TH), taken from Lagarde et al. (2017). The dotted red line represents the minimal values in the model with thermohaline- and rotation-induced extra mixing (TH+ROT), taken from Charbonnel et al. (2017).

first dredge-up slightly less than predicted by the theoretical model. The rotation-induced extra mixing is also not as efficient as theoretically predicted. The same remarks were made in Tautvaišienė et al. (2025) on the basis of open clusters observed in the *Gaia*-ESO survey.

4. Summary and conclusions

In this work, we searched for solar-type pulsations in a sample of 1250 F, G, and K spectral type giants with $V < 8$ mag in a field of about 45 deg radius centred on the TESS continuous viewing zone in the Northern Hemisphere and derived the asteroseismic ages for 218 of them using PARAM and BASTA codes. This sample was used to investigate [Y/Mg] and [C/N] relations with age, taking into account stellar evolutionary stages and the mean galactocentric distances. In this work, the NLTE Mg and Y abundances were used.

Our results can be summarised as follows:

– The [Y/Mg]–age relation exhibits a clear radial dependence across the Galactic disc, with a steeper trend in the outer disc and progressively flatter relations toward the inner disc and the thick disc. In addition, systematic zero-point offsets in [Y/Mg] at fixed age are observed, with the outer disc showing higher [Y/Mg] values than the Solar region, followed by the inner disc and finally the thick disc. These findings highlight differences in star-formation efficiency and chemical enrichment histories. The results are consistent with previous findings of radial variations in *s*-process-to-α-element abundance ratios, as reported for [Y/α] in open clusters by Viscasillas Vázquez et al. (2022) and for [*s*-/Mg] in large samples of disc red giants and main-sequence turn-off and sub-giant-branch stars by Ratcliffe et al. (2024), and confirming the conclusion of Paper II that [Y/Mg] is not a reliable age indicator for thick-disc stars;
– NLTE abundances of Mg, and especially of Y, have to be used to obtain a more precise stellar age evaluation from [Y/Mg] ratios;
– When using [C/N] abundance ratios as stellar age indicators for the first-ascent giant stars and helium-core-burning stars, separate relations have to be used;
– The C/N abundance ratios in the majority of investigated first-ascent RGB stars are affected by the first dredge-up slightly less than predicted by the theoretical models. The rotation-induced extra mixing also is not as efficient as theoretically predicted.

Considering that reliable solar-type pulsations were identified and asteroseismic ages determined for less than 20% of giants in the sample of 1250 stars investigated in this work, methods of alternative stellar age determinations, including chemical clocks, have to be further developed.

Data availability

Full Table A.1 is available at the CDS via https://cdsarc.cds.unistra.fr/viz-bin/cat/J/A+A/708/A250

Acknowledgements. This paper includes data collected by the TESS mission. Funding for the TESS mission is provided by the NASA's Science Mission Directorate. We acknowledge funding from the Research Council of Lithuania (LMTLT, grant No. S-MIP-23-24). We thank the anonymous referee for helpful suggestions.

References

Abdurro'uf, Accetta, K., Aerts, C., et al. 2022, ApJS, 259, 35
Adibekyan, V., Delgado-Mena, E., Figueira, P., et al. 2016, A&A, 592, A87
Adibekyan, V., Gonçalves da Silva, H. M., Sousa, S. G., et al. 2017, Astrophysics, 60, 325
Aerts, C. 2021, Rev. Mod. Phys., 93, 015001
Aguirre Børsen-Koch, V., Rørsted, J. L., Justesen, A. B., et al. 2022, MNRAS, 509, 4344
Alvarez, R., & Plez, B. 1998, A&A, 330, 1109
Arellano-Córdova, K. Z., Esteban, C., García-Rojas, J., & Méndez-Delgado, J. E. 2020, MNRAS, 496, 1051
Asplund, M. 2004, Mem. Soc. Astron. Italiana, 75, 300
Bailer-Jones, C. A. L., Rybizki, J., Fouesneau, M., Demleitner, M., & Andrae, R. 2021, AJ, 161, 147
Beck, P. G., Bedding, T. R., Mosser, B., et al. 2011, Science, 332, 205
Bedding, T. R., Mosser, B., Huber, D., et al. 2011, Nature, 471, 608
Bergemann, M., Collet, R., Amarsi, A. M., et al. 2017, ApJ, 847, 15
Bergemann, M., Hoppe, R., Semenova, E., et al. 2021, MNRAS, 508, 2236
Boeche, C., Siebert, A., Piffl, T., et al. 2014, A&A, 568, A71
Bovy, J. 2015, ApJS, 216, 29
Bovy, J., Allende Prieto, C., Beers, T. C., et al. 2012, ApJ, 759, 131
Brasseur, C. E., Phillip, C., Fleming, S. W., Mullally, S. E., & White, R. L. 2019, Astrocut: Tools for creating cutouts of TESS images, Astrophysics Source Code Library [record ascl:1905.007]
Bressan, A., Marigo, P., Girardi, L., et al. 2012, MNRAS, 427, 127
Casali, G., Magrini, L., Tognelli, E., et al. 2019, A&A, 629, A62
Casali, G., Spina, L., Magrini, L., et al. 2020, A&A, 639, A127
Chabrier, G. 2001, ApJ, 554, 1274
Charbonnel, C., Decressin, T., Lagarde, N., et al. 2017, A&A, 605, A102
Clegg, R. E. S., Lambert, D. L., & Tomkin, J. 1981, ApJ, 250, 262
Cutri, R. M., Wright, E. L., Conrow, T., et al. 2021, VizieR Online Data Catalog: AllWISE Data Release (Cutri+ 2013), VizieR On-line Data Catalog: II/328. Originally published in: IPAC/Caltech (2013)
da Silva, L., Girardi, L., Pasquini, L., et al. 2006, A&A, 458, 609
da Silva, R., Porto de Mello, G. F., Milone, A. C., et al. 2012, A&A, 542, A84
De Silva, G. M., Freeman, K. C., Bland-Hawthorn, J., et al. 2015, MNRAS, 449, 2604
Delgado Mena, E., Moya, A., Adibekyan, V., et al. 2019, A&A, 624, A78
Fredslund Andersen, M., Pallé, P., Jessen-Hansen, J., et al. 2019, A&A, 623, L9
Gaia Collaboration, (Prusti, T., et al.) 2016, A&A, 595, A1
Gaia Collaboration (Brown, A. G. A., et al.) 2018, A&A, 616, A1
Gerber, J. M., Magg, E., Plez, B., et al. 2023, A&A, 669, A43

Gupta, R. P. 2023, MNRAS, 524, 3385
Gustafsson, B., Karlsson, T., Olsson, E., Edvardsson, B., & Ryde, N. 1999, A&A, 342, 426
Gustafsson, B., Edvardsson, B., Eriksson, K., et al. 2008, A&A, 486, 951
Hidalgo, S. L., Pietrinferni, A., Cassisi, S., et al. 2018, ApJ, 856, 125
Hunt, J. A. S., Kawata, D., Grand, R. J. J., et al. 2015, MNRAS, 450, 2132
Iben, Jr., I. 1965, ApJ, 142, 1447
Jenkins, J. M., Twicken, J. D., McCauliff, S., et al. 2016, SPIE Conf. Ser., 9913, 99133E
Jofré, P., Jackson, H., & Tucci Maia, M. 2020, A&A, 633, L9
Jørgensen, B. R., & Lindegren, L. 2005, A&A, 436, 127
Joshi, Y. C. 2007, MNRAS, 378, 768
Jurgenson, C. A., Fischer, D. A., McCracken, T. M., et al. 2014, Proc. SPIE, 9147, 91477F
Jurgenson, C., Fischer, D., McCracken, T., et al. 2016, J. Astron. Instrum., 5, 1650003
Katz, D., Sartoretti, P., Cropper, M., et al. 2019, A&A, 622, A205
Kilic, M., Munn, J. A., Harris, H. C., et al. 2017, ApJ, 837, 162
Kjeldsen, H., & Bedding, T. R. 1995, A&A, 293, 87
Lagarde, N., Robin, A. C., Reylé, C., & Nasello, G. 2017, A&A, 601, A27
Lagarde, N., Reylé, C., Robin, A. C., et al. 2019, A&A, 621, A24
Lagarde, N., Reylé, C., Chiappini, C., et al. 2021, A&A, 654, A13
Lightkurve Collaboration (Cardoso, J. V. d. M., et al.) 2018, Lightkurve: Kepler and TESS time series analysis in Python, Astrophysics Source Code Library [record ascl:1812.013]
Lindegren, L., Bastian, U., Biermann, M., et al. 2021, A&A, 649, A4
Llorente de Andrés, F. 2024, Am. J. Astron. Astrophys., 11, 1
Lu, Y., Pinsonneault, M. H., Ting, Y.-S., et al. 2026, AJ, 171, 38
Luck, R. E. 2018, AJ, 155, 111
Luck, R. E., Andrievsky, S. M., Kovtyukh, V. V., Gieren, W., & Graczyk, D. 2011, AJ, 142, 51
Luri, X., Brown, A. G. A., Sarro, L. M., et al. 2018, A&A, 616, A9
Magrini, L., Vescovi, D., Casali, G., et al. 2021, A&A, 646, L2
Majewski, S. R., Schiavon, R. P., Frinchaboy, P. M., et al. 2017, AJ, 154, 94
Martig, M., Fouesneau, M., Rix, H.-W., et al. 2016, MNRAS, 456, 3655
Masseron, T., & Gilmore, G. 2015, MNRAS, 453, 1855
McDonald, I., & Zijlstra, A. A. 2015, MNRAS, 448, 502
Mints, A., & Hekker, S. 2017, A&A, 604, A108
Molero, M., Magrini, L., Palla, M., et al. 2025, A&A, 694, A274
Mosser, B., Goupil, M. J., Belkacem, K., et al. 2012, A&A, 540, A143
Mosser, B., Benomar, O., Belkacem, K., et al. 2014, A&A, 572, L5
Mosser, B., Vrard, M., Belkacem, K., Deheuvels, S., & Goupil, M. J. 2015, A&A, 584, A50
Mosser, B., Gehan, C., Belkacem, K., et al. 2018, A&A, 618, A109
Nissen, P. E. 2015, A&A, 579, A52
Nissen, P. E. 2016, A&A, 593, A65
Palla, M., Magrini, L., Spitoni, E., et al. 2024, A&A, 690, A334
Paxton, B., Bildsten, L., Dotter, A., et al. 2011, ApJS, 192, 3
Paxton, B., Cantiello, M., Arras, P., et al. 2013, ApJS, 208, 4
Pereira, T. M. D., Kiselman, D., & Asplund, M. 2009, A&A, 507, 417
Pietrinferni, A., Hidalgo, S., Cassisi, S., et al. 2021, ApJ, 908, 102
Planck Collaboration VI. 2020, A&A, 641, A6
Plez, B. 2012, Turbospectrum: Code for spectral synthesis, Astrophysics Source Code Library [record ascl:1205.004]
Randich, S., Gilmore, G., Magrini, L., et al. 2022, A&A, 666, A121
Ratcliffe, B., Minchev, I., Cescutti, G., et al. 2024, MNRAS, 528, 3464
Ricker, G. R., Winn, J. N., Vanderspek, R., et al. 2015, J. Astron. Telesc. Instrum. Syst., 1, 014003
Roberts, J. D., Pinsonneault, M. H., Johnson, J. A., Dubay, L. O., & Johnson, J. W. 2025, ApJ, submitted [arXiv:2509.25321]
Rodrigues, T. S., Girardi, L., Miglio, A., et al. 2014, MNRAS, 445, 2758
Rodrigues, T. S., Bossini, D., Miglio, A., et al. 2017, MNRAS, 467, 1433
Salaris, M., Pietrinferni, A., Piersimoni, A. M., & Cassisi, S. 2015, A&A, 583, A87
Schönrich, R., Binney, J., & Dehnen, W. 2010, MNRAS, 403, 1829
Seabroke, G. M., Fabricius, C., Teyssier, D., et al. 2021, A&A, 653, A160
Sharma, S., Stello, D., Bland-Hawthorn, J., Huber, D., & Bedding, T. R. 2016, ApJ, 822, 15
Shejeelammal, J., Meléndez, J., Rathsam, A., & Martos, G. 2024, A&A, 690, A107
Silva Aguirre, V., Davies, G. R., Basu, S., et al. 2015, MNRAS, 452, 2127
Skrutskie, M. F., Cutri, R. M., Stiening, R., et al. 2006, AJ, 131, 1163
Slumstrup, D., Grundahl, F., Brogaard, K., et al. 2017, A&A, 604, L8
Sneden, C. A. 1973, PhD thesis, The University of Texas at Austin
Soderblom, D. R. 2010, ARA&A, 48, 581
Spina, L., Meléndez, J., Karakas, A. I., et al. 2016, A&A, 593, A125
Spina, L., Meléndez, J., Karakas, A. I., et al. 2018, MNRAS, 474, 2580
Spitoni, E., Recio-Blanco, A., de Laverny, P., et al. 2023, A&A, 670, A109
Spoo, T., Tayar, J., Frinchaboy, P. M., et al. 2022, AJ, 163, 229
Spoo, T., Thomas, K., Toguchi-Tani, E. K., et al. 2025, AJ, 170, 333
Stello, D., & Sharma, S. 2022, RNAAS, 6, 168
Storm, N., & Bergemann, M. 2023, MNRAS, 525, 3718
Storm, N., Barklem, P. S., Yakovleva, S. A., et al. 2024, A&A, 683, A200
Sysoliatina, K., Just, A., Golubov, O., et al. 2018, A&A, 614, A63
Tautvaišienė, G., Mikolaitis, Š., Drazdauskas, A., et al. 2020, ApJS, 248, 19
Tautvaišienė, G., Viscasillas Vázquez, C., Mikolaitis, Š., et al. 2021, A&A, 649, A126
Tautvaišienė, G., Mikolaitis, Š., Drazdauskas, A., et al. 2022, ApJS, 259, 45
Tautvaišienė, G., Drazdauskas, A., Mikolaitis, Š., et al. 2025, A&A, 703, A4
Titarenko, A., Recio-Blanco, A., de Laverny, P., Hayden, M., & Guiglion, G. 2019, A&A, 622, A59
Tucci Maia, M., Ramírez, I., Meléndez, J., et al. 2016, A&A, 590, A32
Valle, G., Dell'Omodarme, M., Prada Moroni, P. G., & Degl'Innocenti, S. 2018, A&A, 609, A58
Viscasillas Vázquez, C., Magrini, L., Casali, G., et al. 2022, A&A, 660, A135
Viscasillas Vázquez, C., Tautvaišienė, G., Pakštienė, E., et al. 2025, Galaxies, 13, 136
Vitali, S., Slumstrup, D., Jofré, P., et al. 2024, A&A, 687, A164
Xiang, M., & Rix, H.-W. 2022, Nature, 603, 599

Appendix A: Machine readable tables of results

Table A.1. Parameters of stars.

Col	Label	Units	Explanations
1	ID	–	Tycho-2 catalogue identification
2	Age_PARAM	Gyr	Asteroseismic age determined using PARAM(v.1.5)
3	e_lo_Age_PARAM	Gyr	Lower uncertainty (68% credible interval) in the age determination with PARAM
4	e_up_Age_PARAM	Gyr	Upper uncertainty (68% credible interval) in the age determination with PARAM
5	Age_BASTA	Gyr	Asteroseismic age determined using BASTA
6	e_lo_Age_BASTA	Gyr	Lower uncertainty (16th quantile) in the age determination with BASTA
7	e_up_Age_BASTA	Gyr	Upper uncertainty (84th quantile) in the age determination with BASTA
8	Age_Asteroseismic	Gyr	Asteroseismic age, averaged when both PARAM and BASTA age values available
9	$\nu_{\rm max}$	μHz	Frequency at maximum power
10	$e\_\nu_{\rm max}$	μHz	Uncertainty in frequency at maximum power
11	$\Delta\nu$	μHz	Large frequency separation
12	$e\_\Delta\nu$	μHz	Uncertainty in large frequency separation
13	Mass_PARAM	$M_\odot$	Stellar mass determined using PARAM(v.1.5)
14	e_lo_Mass_PARAM	$M_\odot$	Lower uncertainty (68% credible interval) of mass determined with PARAM
15	e_up_Mass_PARAM	$M_\odot$	Upper uncertainty of mass (68% credible interval) determined with PARAM
16	Mass_BASTA	$M_\odot$	Stellar mass determined with BASTA
17	e_lo_Mass_BASTA	$M_\odot$	Lower uncertainty (16th quantile) of mass determined with BASTA
18	e_up_Mass_BASTA	$M_\odot$	Upper uncertainty (84th quantile) of mass determined with BASTA
19	Mass_Asteroseismic	$M_\odot$	Asteroseismic mass, averaged when both PARAM and BASTA mass values available
20	[Mg/H]LTE	dex	LTE magnesium abundance from Paper I or Paper III
21	[Mg/H]NLTE	dex	NLTE magnesium abundance
22	[Y/H]LTE_1	dex	LTE yttrium abundance from Paper II
23	[Y/H]LTE_2	dex	LTE yttrium abundance determined in this work
24	e_[Y/H]LTE_2	dex	Uncertainty in LTE yttrium abundance determined in this work
25	[Y/H]NLTE	dex	NLTE yttrium abundance
26	[C/N]	dex	[C/N] ratio from Paper I or Paper III
27	C/N	–	Carbon-to-nitrogen abundance ratio from Paper I or Paper III
28	Evol	–	Evolutionary stage (BB or AB – stars below or above the RGB luminosity bump, respectively. RC – Clump stars)
29	Evol method	–	Method of the evolutionary stage determination. 1 – if determined purely from asteroseismic data, 2 – if isochronal information was involved
30	Disc	–	0 – Thin disc, 1 – Thick disc; taken from Paper I or Paper III

Notes. Full table is available at the CDS.